



# One-pot synthesis of NH<sub>2</sub>-MIL-101(Fe) and $\alpha$ – Fe<sub>2</sub>O<sub>3</sub> composite as efficient heterojunction for multifunctional photocatalytic membranes: Towards zero waste generation

Karthikeyarajan Vinothkumar, R Geetha Balakrishna\*

Centre for Nano and Material Sciences, Jain (Deemed-to-be) University, Bangalore 562112, Karnataka, India



## ARTICLE INFO

**Keywords:**  
NH<sub>2</sub>-MIL-101(Fe)  
 $\alpha$ -Fe<sub>2</sub>O<sub>3</sub>  
MOF chemistry  
Photocatalysis  
Water-treatment

## ABSTRACT

Here in, one-pot synthesis of amine functionalized iron-based Metal-Organic Framework (MOF) namely NH<sub>2</sub>-MIL-101(Fe) is systematically tuned such that it also results in formation of morphology-oriented iron-oxide ( $\alpha$ -Fe<sub>2</sub>O<sub>3</sub>) along with MOF, without adding any additional precursor. Ligand deficiency facilitates the free amine group of ligands to drive the formation of metal oxide (MO). This composite of MO and MOF behaves as a heterojunction that efficiently separates charge carriers and allows good photocatalytic activity, with more than 95 % degradation of methylene blue (MB) dye. The composite was then integrated into nanofiber membranes for water treatment, it resulted in overall 94 % rejection, with 20 % of MB being degraded simultaneously during this rejection and, this can be considered as fairly good for an emerging process that comprises of simultaneous degradation and separation. The new thermally stable and self-cleaning heterojunction MOF membranes developed in this study have sparked hopes as promising materials for near to zero waste generation in water treatment.

## 1. Introduction

The iconic development of metal-organic frameworks (MOFs) (Yagi et al., 1995) [1,2] over the past two decades has created an enormous interest in reticular chemistry. MOFs are highly crystalline and porous materials made of organic linkers as primary building units (PBU) and metal ions as secondary building units (SBU) [3]. MOFs built on well-defined secondary building units (SBUs) and rigid organic linkers with high symmetry, largely have predictable topology, but sometimes become unpredictable because of the various connectivity of these PBU nodes with SBU [4]. In practice, the manipulation of coordination between metal cations and ligands is crucial to construct MOFs with various morphological and structural diversities [5–8]. The metal cations can effectively alter the topology of the co-ordination nodes while the ligands can completely influence the MOF composition itself. Thus, crystallization can appropriately be tuned during synthesis to obtain the desired structure growth and orientation. So, a variety of new topologies have been observed for MOFs unlike other crystalline materials [9,10], and such variations can surprisingly result in enhanced properties [11, 12]. For instance, stability of MOFs has been improved sufficiently by varying PBU (quantity or length) [13]. Mixed ligand and mixed metal

strategy have been attempted extensively to achieve combined functions that includes selective adsorption, reversible adsorption and photocatalytic degradation of pollutants in wastewater [14–16]. Even though the performance of MOFs is observed to increase by bi-ligand/bimetal strategy, the cumbersome multi steps involved makes it difficult to have control over structure, in addition to high-costs being involved. It is also possible that accidental mismatch of building blocks can sometimes lead to new structural diversity [17] surprisingly enriched with more than one composition that can oppose each other and offer resistance.

Iron (Fe) based MOFs are extensively used in wastewater treatments such as adsorption [18], membrane separation [19], photocatalytic degradation [20], photo-Fenton process [21] due to its robust nature in the hazardous environment, higher selectivity and adsorption capacity and, this has motivated us to experiment the synthesis of Fe-MOFs via mismatch of PBU and SBU as an in-situ modification strategy to obtain a composite of Fe-MOF. On the other hand, ex-situ attempts have been made to make composites of Fe-MOF with other functional materials. One such effort is functionalization of Fe-MOF using graphene which has improved the photocatalytic degradation of dye pollutants [22]. Ex-situ integration of support materials with MOFs to form composites so as to improve the efficiency is a multistage process [16], sometimes

\* Corresponding author.

E-mail address: [br.geetha@jainuniversity.ac.in](mailto:br.geetha@jainuniversity.ac.in) (R.G. Balakrishna).

superficial [23] and also sluggish that significantly increases the cost and restricts practical usage [24].

In the present work, low cost and simple way to improve Fe-MOF performance and stability is attempted by a) amine ( $\text{NH}_2$ ) functionalization and b) in-situ integration of metal oxide [25]. Dual light excitation pathways one, in which  $\text{NH}_2$  functionality induces an electron transfer to the Fe centers and the other one being direct excitation of Fe-O clusters ( $\text{Fe}^{3+}$  to  $\text{Fe}^{2+}$ ) [26] makes the present system behave as multifunctional. PBU and metal precursor compositions have been tuned for the first time to obtain Fe-MOF along with metal oxide (MO). Our strategy of using precursor deficiency offers various insights into understanding of construction of these in-situ built composite of MO-MOFs and opens new directions in reticular chemistry. It involves facile single pot synthesis of spherical  $\alpha\text{-Fe}_2\text{O}_3$  along with  $\text{NH}_2\text{-MIL-101(Fe)}$ . The control on nucleation, growth and morphology of MOFs in these processes has been systematically carried out and analyzed. Further, synthesis of only  $\alpha\text{-Fe}_2\text{O}_3$  under same conditions without the use of any linker, for comparison, adds another perspective to the work and this synthesis method is found to have created high oxygen vacancy, beneficial for improving the photocatalytic performance [27]. Various morphologies of  $\alpha\text{-Fe}_2\text{O}_3$  have otherwise been reported by W. Zheng et al. and L. Qu et al. using ionic liquid [28] and basic medium [29] as morphology influencers. Even though Fe-MOFs are a potential candidate for photocatalytic wastewater treatment, concern with respect to its practical implementation due to low photocatalytic activity, catalyst recovery, and recyclability in addition to itself being secondary pollutant exists. Hence the obtained composite of  $\text{NH}_2\text{-MIL-101(Fe)}$  and  $\alpha\text{-Fe}_2\text{O}_3$  is subsequently embedded in PAN and electro-spun as nanofibers for its extended applications namely self-cleaning of membranes and simultaneous separation and photocatalytic degradation of multiple pollutants.

## 2. Experimental section

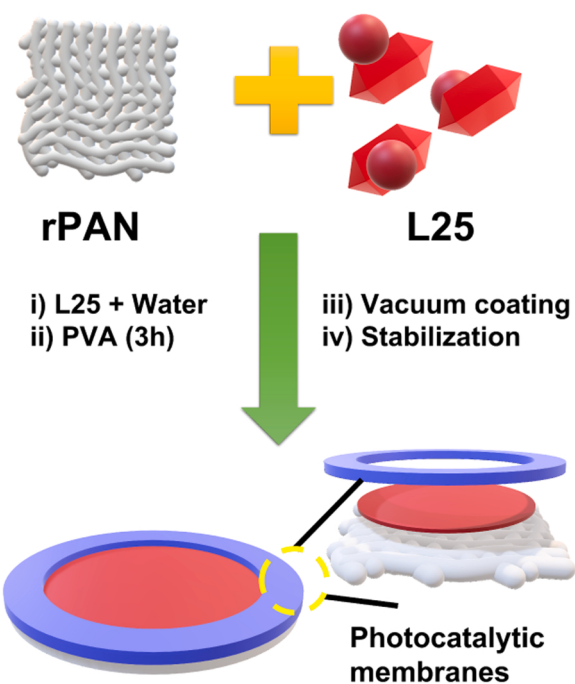
### 2.1. Materials

Iron (III) chloride hexahydrate ( $\text{FeCl}_3\bullet6\text{H}_2\text{O}$ , 99 %), 2-aminoterephthalic acid ( $\text{NH}_2\text{-BDC}$ , 99 %), polyacrylonitrile (PAN)  $M_w$  150,000, *N,N*-dimethylformamide (DMF, 99.8 %), poly (vinyl alcohol) (PVA,  $M_w$  146,000–186,000, 87–89 % hydrolyzed), potassium dichromate ( $\text{K}_2\text{Cr}_2\text{O}_7$ , 99 %), *tert*-butyl alcohol (99.5 %) is procured from Sigma Aldrich, citric acid anhydrous (99 %), Hydrazine hydrate (80 %), bisphenol A (BPA, 97 %), ethylenediaminetetraacetic acid (EDTA, 99 %), silver nitrate ( $\text{AgNO}_3$ , 99 %), and potassium iodide (KI) from SRL chemicals, *para*-benzoquinone (*p*-BQ, 97 %) from TCI chemicals hydrogen peroxide ( $\text{H}_2\text{O}_2$ , 30 %) from Merck. All the chemicals were used without any pre-treatment. Disposable syringe filter having a PTFE microfiltration membrane (pore size: 0.2  $\mu\text{m}$ ), AXIVA is purchased from bio mall.

Detailed experimental section that includes methods for characterization, instrumentation details, synthesis of PAN nanofibers, functionalization of PAN nanofibers (Fig. S1), photocatalytic experimental setup, and membrane performance study calculations is provided in supplementary section.

### 2.2. Synthesis of MOFs

$\text{NH}_2\text{-MIL-101(Fe)}$  MOF was prepared as per literature without any further modification [30]. Shortly, 5 mmol of iron chloride hexahydrate ( $\text{FeCl}_3\bullet6\text{H}_2\text{O}$ ) and 2.5 mmol of 2-aminoterephthalic acid were dissolved in 60 mL of *N,N*-dimethylformamide (DMF). Then the solution was transferred into teflon-lined autoclave and heated at 110 °C for 24 h. The resulting precipitate was centrifuged and washed with DMF and ethanol (three times) to remove residual impurities. The purified product was then dried in vacuum oven at 120 °C overnight. The obtained dark brown MOF particles were termed as 'normal MOF'.



**Scheme 1.** Representation of fabrication of photocatalytic membrane using electrospun nanofibers of rPAN.

The above stoichiometric ratio of precursors is considered as 1:1 ratio. For modifications, stoichiometric deficiency was created in the synthesis process. Briefly, same protocol was followed but with the different ratio of SBU and PBU (0.25, 0.50 and 0.75) named as M25, M50, M75, L25, L50 and L75. Interestingly, significant color difference between samples could be observed and the photographs of all the samples are presented in Fig. S2. The synthesis of conventional  $\text{NH}_2\text{-MIL-101(Fe)}$ , DMF mediated synthesis of  $\alpha\text{-Fe}_2\text{O}_3$  without ligand (FWL) and ligand deficient synthesis of L25 ( $\text{NH}_2\text{-MIL-101(Fe)} + \alpha\text{-Fe}_2\text{O}_3$ ) is schematically represented in Fig. S3.

### 2.3. Photocatalytic membrane fabrication

Photocatalytic membranes were fabricated by vacuum filtration as shown in Scheme 1. Briefly, 20 mg of L25 photocatalytic material was added to 50 mL of deionized water containing 1 % of poly (vinyl alcohol) (PVA). The mixture was then stirred for 3 h and sonicated for 0.5 h to obtain a fine dispersion. PVA was stabilized according to our earlier procedure, using citric acid as cross-linker [31], before introducing L25 into PVA solution. The above mixture was poured through the vacuum filtration setup supported with rPAN placed on the top of polyester support. On applying high vacuum, a uniformly coated colored membrane containing L25 was visible and this was carefully peeled off from the support sheet without disturbing the coating and then dried under vacuum at 80 °C overnight for stabilization. The coated photocatalytic membrane was very strong and does not wear out even on scratching. This was used further for separation and degradation of methylene blue (MB), chromium (VI) reduction (Cr (VI)) and bisphenol-A (BPA).

## 3. Results and discussion

### 3.1. Structural analysis

#### 3.1.1. XRD and ATR-IR studies

X-Ray Diffraction (XRD) patterns recorded for deficient and normal MOF are given in Fig. 1 (a) and Fig. S4 (a). Diffraction peaks at 2 theta equal to 9.3°, 16.6°, 18.6°, 21.6°, 25.8° and 28.2° in Fig. S4 (a) are in agreement with the literature [30] and confirms the formation of

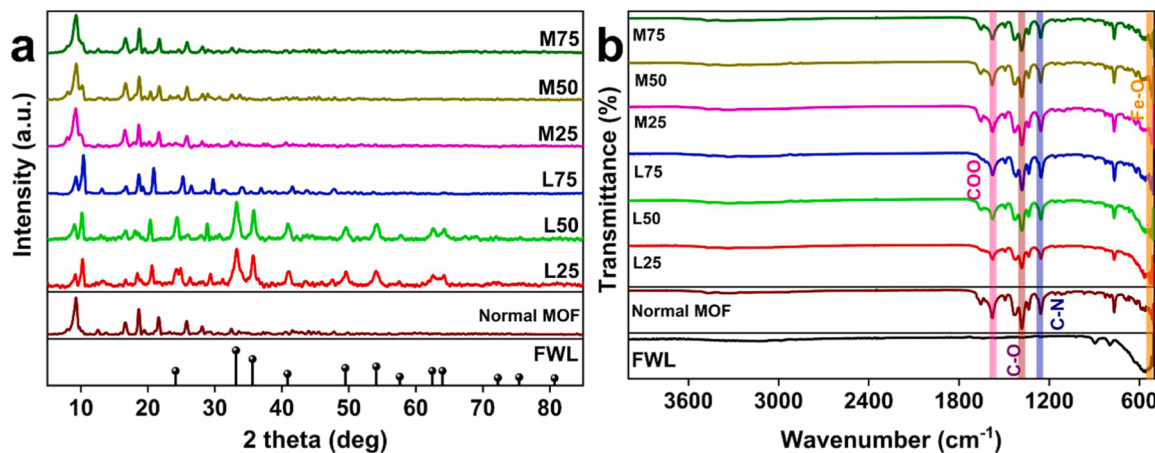
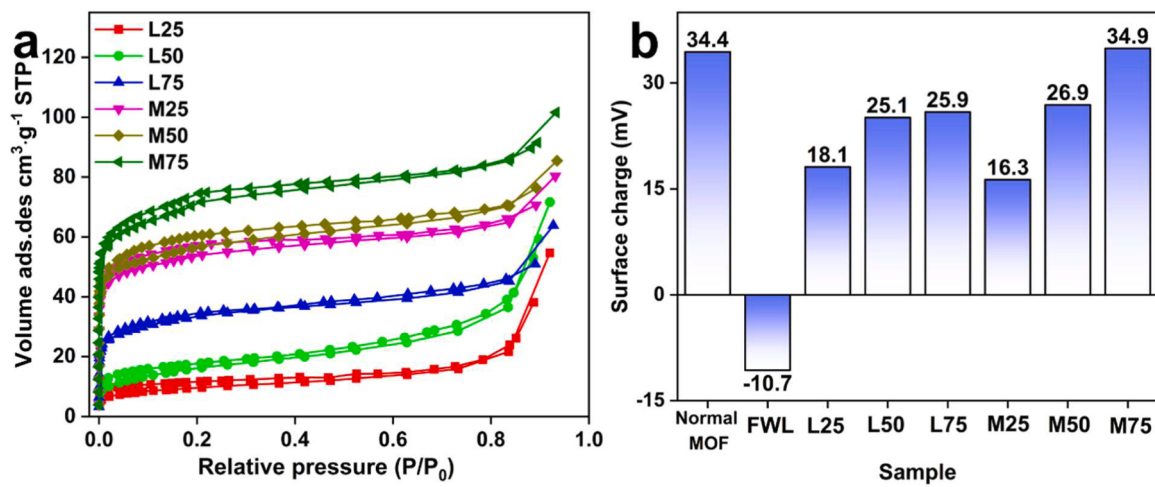


Fig. 1. (a)XRD and (b)ATR-IR spectra of the synthesized materials.

Fig. 2. (a) BET N<sub>2</sub> adsorption/desorption isotherms and (b) surface charge of the synthesized materials.

Fe-MOF. PBU deficient MOFs have been identified with new peaks in the range 24–64° (obvious in L25 and L50) as shown in Fig. 1 (a) and could be surprisingly indexed to standard (reference)  $\alpha$ -Fe<sub>2</sub>O<sub>3</sub>, JCPDS card (33-0664). Deficiency of ligand or excess of FeCl<sub>3</sub>·6 H<sub>2</sub>O leads to the formation of  $\alpha$ -Fe<sub>2</sub>O<sub>3</sub> along with MOF particles. For comparison and further elucidation of mechanism, separate  $\alpha$ -Fe<sub>2</sub>O<sub>3</sub> nanoparticles were synthesized under the same conditions but without the use of linker (termed as FWL hence) and analyzed. Its XRD pattern, in Fig. S4(b) shows peaks at 24.1°, 33.1°, 35.6°, 40.8°, 49.4°, 54.0°, 57.5°, 62.4°, and 63.9° that correspond to planes (012), (104), (110), (113), (024), (116), (018), (214), and (300) and matches with the standard reference as mentioned above. The additional peaks that arise in PBU deficient MOFs, indicate the presence of  $\alpha$ -Fe<sub>2</sub>O<sub>3</sub>. PBU deficient MOFs show very little changes in peaks that were assigned to MOF as shown in Fig. 1 (a). Fig. S5, depicts the zoomed in patterns and peak at 9.2° appears to deviate and give rise to one more peak at 10.2° and, at higher PBU concentration this peak shifts to 10.4° while peak deviation (at 9.2°) is restored. XRD peaks analyzed for SBU deficient MOFs did not depict any significant changes. PBU deficiency is thus observed to significantly influence the crystal structure of MOF in comparison to SBU.

Attenuated total reflection – Infra Red (ATR-IR) spectra of normal MOF and FWL are shown in Fig. S6(a)-(b) and that of deficient MOFs in Fig. 1 (b). The majority of peaks in normal MOF represent benzene carboxylate of ligands. The band at 1580 cm<sup>-1</sup> and 1381 cm<sup>-1</sup> represent asymmetric COO<sup>-</sup> and C-O vibrations of carboxylates respectively [32]. A strong peak at 562 cm<sup>-1</sup> represents the Fe-O (octahedral sites)

stretching in normal MOF [33]. Further the N-H and C-N stretch of primary amine present in the ligand were observed at around 3300 (dual) and 1257 cm<sup>-1</sup> respectively (Fig. S6(a)) [34] and they remain absent in Fig. S6(b) corresponding to FWL and, a broad peak at ~3200 cm<sup>-1</sup> in it correspond to O-H (may be due to adsorbed water). For deficient MOFs, all the characteristic peaks mentioned above for normal MOF including the high intense Fe-O peak at 521 cm<sup>-1</sup> appear undisturbed. However, the intensity of benzene carboxylate and N-H of amine stretching appear to have reduced significantly in PBU deficient MOFs. PBU deficient materials particularly L25 and L50 exhibit broad noisy peak in the range of 515–570 cm<sup>-1</sup> much similar to  $\alpha$ -Fe<sub>2</sub>O<sub>3</sub> which is not found in other deficient materials. Further as the PBU deficiency decreases, the intensity of the carboxylate and N-H peaks increases and the broad band around 550 cm<sup>-1</sup> disappears which confirms the absence of  $\alpha$ -Fe<sub>2</sub>O<sub>3</sub> in L75 and in other metal deficient MOFs.

### 3.1.2. Surface analysis

Surface area and surface charge analysis of deficient MOFs were analyzed by Brunauer-Emmett-Teller (BET) and zeta potential measurements respectively and the results are depicted in Fig. 2 (a)-(b) and Table S1. In addition, BET adsorption isotherm and pore size distribution curves of normal MOF and FWL are given in Fig. S7(a)-(c). It can be clearly seen that normal MOF has higher surface area of 336.87 m<sup>2</sup>/g which emphasizes type – I(b) isotherm with wide micropores, narrow mesopores and mean pore diameter of 2.47 nm [35]. Monolayer molecular volume (V<sub>m</sub>) of 77.40 cm<sup>3</sup> (STP)/g further confirms the high

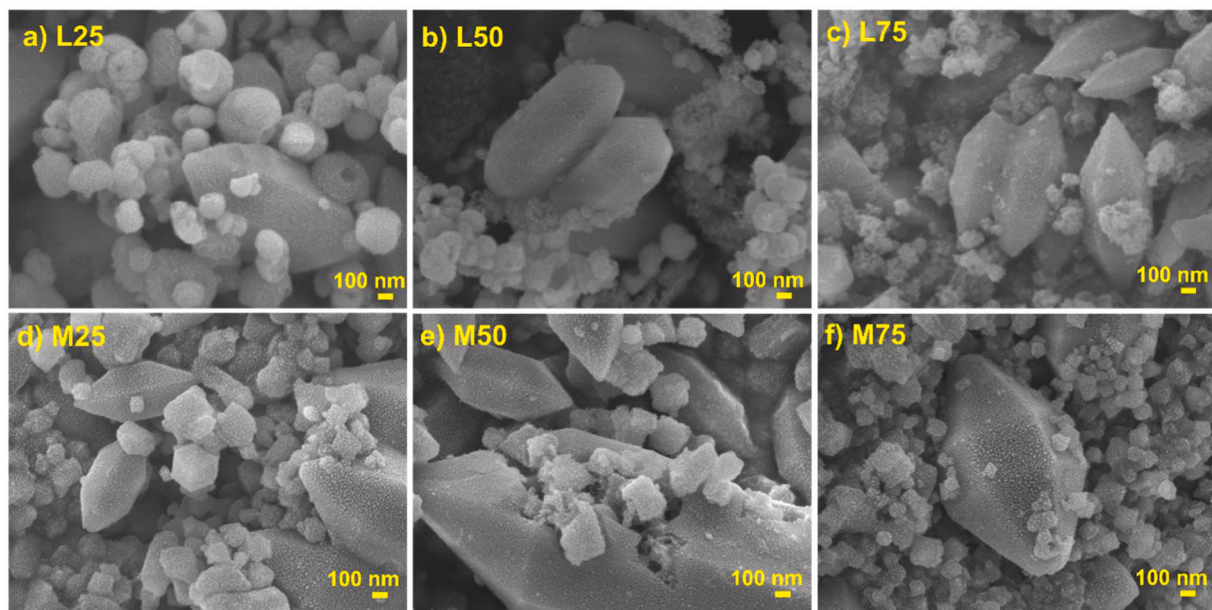


Fig. 3. FESEM images of deficient MOFs.

porous nature of material. FWL, shows type – IV(b) isotherm with mesoporous nature, possessing mean pore diameter of 4.30 nm (calculated from BJH plot) and lesser pore volume of 0.028 cm<sup>3</sup>/g.  $V_m$  for the metal oxide is only 5.99 cm<sup>3</sup>(STP)/g. Fig. S7(d) shows mean pore diameter calculated from BJH plots for all other deficient MOFs. As PBU deficiency decreases (L25 >L50 >L75) the surface area ( $a_s$ ) increases along with increase in total pore volume, monolayer molecular volume ( $V_m$ ), and a decrease in pore diameter and, they all show type - IV(b) mesoporous nature similar to FWL. Similar trend of increasing surface area (M25 <M50 <M75) has been observed with decrease in metal deficiency. However, the obtained isotherm for metal deficiency is similar to normal MOF, type - I(b). Highest pore diameter in L25 clearly indicates the combination of completely two different morphology materials. It can thus be concluded that the influence of primary building units (PBU) in the reaction mixture is higher compared to secondary building unit (SBU).

Zeta potential analysis was done to measure the surface charge and elucidate the change in chemistry that occurs during deficient synthesis of MOFs. The surface charge of normal MOF is + 34.4 mV while that of FWL is – 10.7 mV. PBU deficient MOFs show substantial decrease in surface charge due to the presence of negatively charged  $\alpha$ -Fe<sub>2</sub>O<sub>3</sub>. The increase in positive charge with decrease in PBU deficiency indicates the

reduced quantity of  $\alpha$ -Fe<sub>2</sub>O<sub>3</sub>. For SBU deficient MOFs, the surface charge enhances with decrease in deficiency of metal sites and almost reaches the surface charge of normal MOF. Uncoordinated ligand (excess) due to metal deficiency can impart negative charge and thus the low positive charge of M25 can be explained. However, charge increases further because of increase in  $Fe^{3+}$ . The change in surface charge of the components present in them thus leads us to infer that  $\alpha$ -Fe<sub>2</sub>O<sub>3</sub> is formed along with normal MOF in ligand deficient synthesis and not in metal deficient synthesis of MOFs.

### 3.1.3. Morphology and size analysis

The field emission scanning electron microscopy (FESEM) images of normal MOF and FWL are shown in Fig. S8(a)-(b) and that of deficient MOFs in Fig. 3 (a)-(f). Normal MOF shows octahedral morphology which is consistent with the literature [34], while FWL shows an irregular morphology. Deficient MOF L25, shows many dented spheres of  $\alpha$ -Fe<sub>2</sub>O<sub>3</sub> along with few hexagonal-micro spindle of NH<sub>2</sub>-MIL-101(Fe) due to excess metal sites and these spheres reduce with increase in PBU concentration. Two different morphologies in the composite hence result in higher pore diameter. SBU deficient MOFs particularly M75 depict octahedral particles along with very few hexagonal micro-spindle, indicating near to complete growth of NH<sub>2</sub>-MIL-101(Fe), with

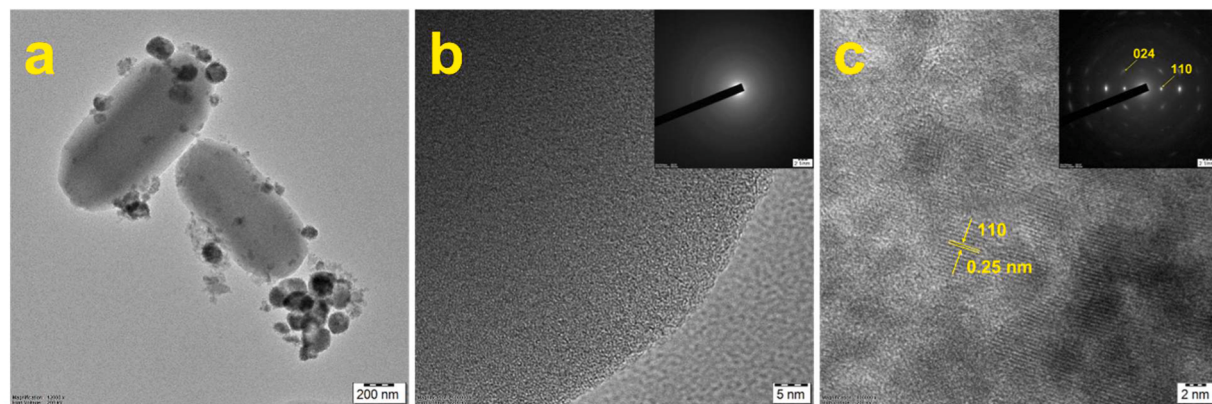


Fig. 4. (a) TEM image of L25 (b) HRTEM image of NH<sub>2</sub>-MIL-101(Fe) region in L25, inset: its SAED pattern (c) HRTEM image of  $\alpha$  – Fe<sub>2</sub>O<sub>3</sub> region in L25, inset: its SAED pattern.

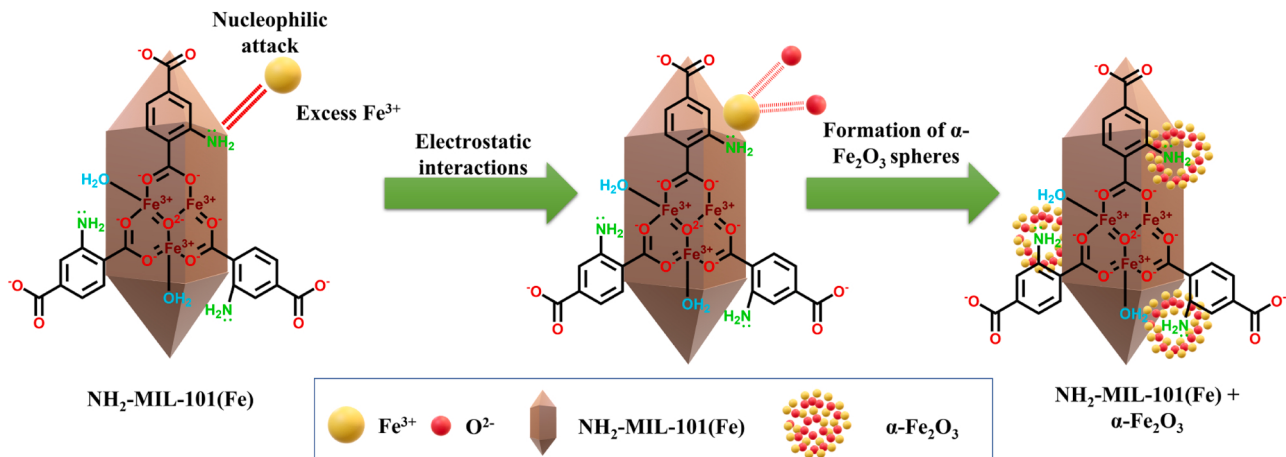


Fig. 5. Plausible mechanism for formation of  $\alpha$  –  $\text{Fe}_2\text{O}_3$  spheres during ligand deficient synthesis.

availability of metal sites. PBU plays an important role in achieving this octahedral morphology, which cannot be found in PBU deficient MOFs. Even with the shortage of metal precursor, the ligands can competitively coordinate to the vacant metal sites. As mentioned earlier the structure growth and orientation can be tuned during crystallization, which we believe gets incomplete to form micro-spindles with insufficient PBU. So extra metal sites tend to form metal oxides in PBU deficient materials. However, a complete octahedral geometry is possible only with optimized ratio of PBU and SBU where only octahedrons will be formed as can be seen in normal MOF images Fig. S8(a). Difference in stoichiometry of PBU to SBU could influence the structural morphology as shown in the 2D schematic representation of Fig. S8(c). Ligand deficient MOFs show longer facets, have micro-spindle like structure wherein, a oval-shape with well-angulated six facets was visible. The nodes at both ends appeared blunt and short. Meanwhile, metal-ion deficient MOFs facet length is compressed, and rectangular facet becomes square and it slowly diminishes to give octahedral geometry with longer region at nodes as deficiency diminishes.

#### 3.1.4. TEM analysis

Transmission Electron Microscopy (TEM) and high-resolution TEM (HRTEM) captured to further analyze the structure and morphology of L25 and normal MOF, FWL are presented in Fig. 4 and Fig. S9 respectively. Fig. 4(a) shows  $\alpha$  –  $\text{Fe}_2\text{O}_3$  spheres along with micro-spindles of  $\text{NH}_2\text{-MIL-101(Fe)}$ . HRTEM at MOF region shows no fringes or specific selected area electron diffraction (SAED) pattern as can be seen in Fig. 4 (b). While the dented sphere region in Fig. 4(c) and its inset depict lattice fringes of 0.25 nm (110) corresponding to  $\alpha$  –  $\text{Fe}_2\text{O}_3$  [36]. Normal MOF

in Fig. S9(a) evidences the octahedral morphology with a size of ~400 nm and  $\alpha$  –  $\text{Fe}_2\text{O}_3$  in Fig. S9(e) depicts lattice fringes with  $d$ -spacing of 0.25 nm (110) (JCPDS - 33-0664). Fig. S9(d), illustrates its square morphology with very small sizes around < 20 nm and exhibit polycrystallinity (Fig. S9(f)). However, use of linker renders that aggregated sphere morphology, and that seem to provide it with good properties like stability. It is interesting to note that these spheres are attracted to MOF particles particularly at nodes.

#### 3.1.5. Formation of $\alpha$ - $\text{Fe}_2\text{O}_3$ spheres

Various morphologies of  $\alpha$ - $\text{Fe}_2\text{O}_3$  have been reported by W. Zheng et al. and L. Qu et al. using ionic liquid [28] and basic medium [29] as morphology influencers. Our approach of PBU deficiency during normal MOF synthesis leads to the formation of spherical  $\alpha$ - $\text{Fe}_2\text{O}_3$  without adding any extra surface modifiers unlike previously reported [28]. The formation of spherical  $\alpha$ - $\text{Fe}_2\text{O}_3$  in L25 material could be because of the influence of easily available primary amine group from the 2-amino-terephthalic acid of ligand. Primary amine group acts as a nucleophile and attracts all excess  $\text{Fe}^{3+}$  which forms an aggregation of Fe-O (with oxygen of DMF), under specified temperature (110 °C) and pressure. This process can thus be envisaged as a step wise nucleation, initiated by ligand and on heating at 120 °C under vacuum eliminates trapped carbon and curls into spheres with sizes more than 200 nm. The same DMF mediated synthesis of obtaining  $\alpha$ - $\text{Fe}_2\text{O}_3$  without ligand did not result in spherical morphology but just nanoparticles of sizes equal to ~20 nm. TEM images too support this wherein most of the  $\alpha$ - $\text{Fe}_2\text{O}_3$  dangles around micro-spindles of  $\text{NH}_2\text{-MIL-101(Fe)}$  particles [Fig. 4 (a)]. Azuma et al. also used DMF solvent in synthesis of  $\alpha$ - $\text{Fe}_2\text{O}_3$  to reduce the particle size

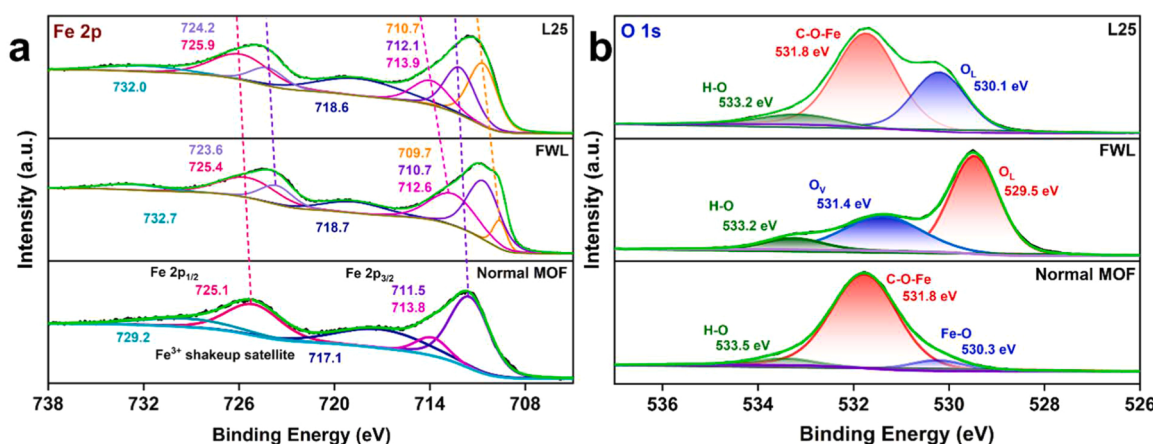


Fig. 6. High-resolution core XPS spectra of (a) Fe 2p (b) O 1s.

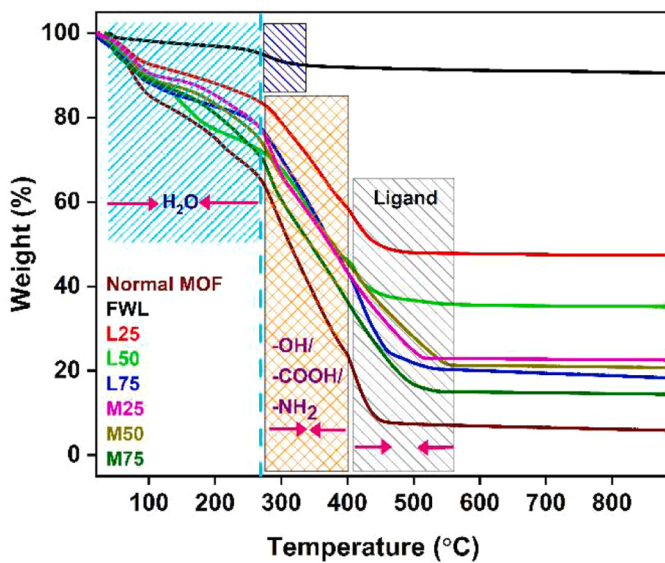


Fig. 7. TGA for synthesized materials.

and achieved mono dispersion of  $\alpha$ -Fe<sub>2</sub>O<sub>3</sub> with very small particle sizes of 2–5 nm [37]. All these findings indicate the strong importance of ligand in formation of  $\alpha$ -Fe<sub>2</sub>O<sub>3</sub> as spheres in L25; the plausible mechanism is illustrated in Fig. 5.

### 3.1.6. XPS analysis

The elemental compositions and surface chemical states of as prepared samples of normal MOF, FWL and L25 were analyzed by X-ray photoelectron spectroscopy (XPS). Fig. S10(a) represents the survey spectrum of normal MOF, FWL and L25 and shows the existence of C 1 s, O 1 s, N 1 s and Fe 2 p. All peaks of Fe 2 P spectra of normal MOF and FWL in Fig. 6 (a) match well with the existing reports [38,39]. Notably, peaks in L25 corresponding to both these components appear to have shifted substantially to higher binding energy (indicated by dash), indicating electron distribution over Fe due to electrostatic interaction between spheres of  $\alpha$ -Fe<sub>2</sub>O<sub>3</sub> and micro spindles of MOF. More information can be extracted from O1s spectrum in Fig. 6 (b), where the FWL depicts vacancies because of which this defect material shows photo instability although it possesses higher photocatalytic activity (can be seen in ahead sections). L25 shows lattice oxygen much similar to  $\alpha$ -Fe<sub>2</sub>O<sub>3</sub>, in addition to Fe-O bond of MOF (C-O-Fe), again confirming both entities in L25 [40]. However, N1s peaks in Fig. S10(b), do not show any difference in spectra of L25 and normal MOF, although some interaction between amine of ligand and Fe<sup>3+</sup> is predicted. So, it can be

concluded that presence of 'N' only initiates the formation of  $\alpha$ -Fe<sub>2</sub>O<sub>3</sub> which on heating at 120 degrees become two different entities; however, they remain attracted to each other because of high negative surface charge of FWL (-10.7 mV) and high positive charge of MOF particle (34.4 mV). Similarly, no extra information or difference between entities could be identified in comparative C1s spectra illustrated in Fig. S10(c).

### 3.1.7. TGA

Thermogravimetric analysis (TGA) performed for all samples are depicted in Fig. 7 and they illustrate a three-step weight loss process for all MOFs. The first weight loss around 50–270 °C correspond to water molecules adsorbed on surface and also in pores of MOFs. The second step weight loss from 270 to 400 °C could be attributed to the elimination of functional groups namely -OH, -COOH, -Cl and NH<sub>2</sub> group of ligands. Final weight loss after 400 °C indicates the complete degradation of ligands and information derived from this suggest that the deficiency plays a crucial role in increasing the stability of the material. This can be confirmed by observing the FWL plot. Only two identical weight losses (only 9 %), that of surface adsorbed (~100 °C) and chemically (< 200 °C) adsorbed water molecules can be seen in FWL which contains  $\alpha$ -Fe<sub>2</sub>O<sub>3</sub>. Ligand deficiency leads to formation of  $\alpha$ -Fe<sub>2</sub>O<sub>3</sub> in L25 thus making it thermally very stable.

### 3.1.8. Bandgap analysis

Light harvesting property of this material was important as the end application of this is photocatalytic degradation. Bandgap analysis and band edge potential for the synthesized MOFs and reference material are analyzed via UV-Vis DRS, Tauc and Mott Schottky plots (MS) respectively and the obtained plots are shown in Fig. S11(a)-(i) and S12(a)-(h). All MOF materials possess visible light absorption and band gap ranges from 1.59 to 1.75 eV, and FWL depicts a band gap of 2.24 eV. Mott Schottky analysis indicate all materials to be n-type (positive slope) semiconductor. Therefore, their conduction band (CB) potential would be + 0.205 V higher than the flat band potential estimated using the MS plots, and the valence band (VB) potential is calculated using the formula  $E_{VB} = E_g + E_{CB}$  [41]. VB and CB for these materials are illustrated in Fig. 8 (a). Deficient MOF materials show comparatively lower oxidation potential.

It is well known that surface hydrophilicity of a material enables more OH adsorption on the surface and tends to enhance photocatalysis [42]. Hydrophilic nature is estimated through its contact angle, measured using goniometer and the obtained digital photographic images are given in Fig. S13(a)-(h), with results being depicted in Fig. 8 (b). L25 and M25 show the lowest contact angle of 20.9° and 26.8° indicating its higher hydrophilicity compared to others. Deficiency of PBU/SBU in these materials is the main reason behind this or uncoordinated

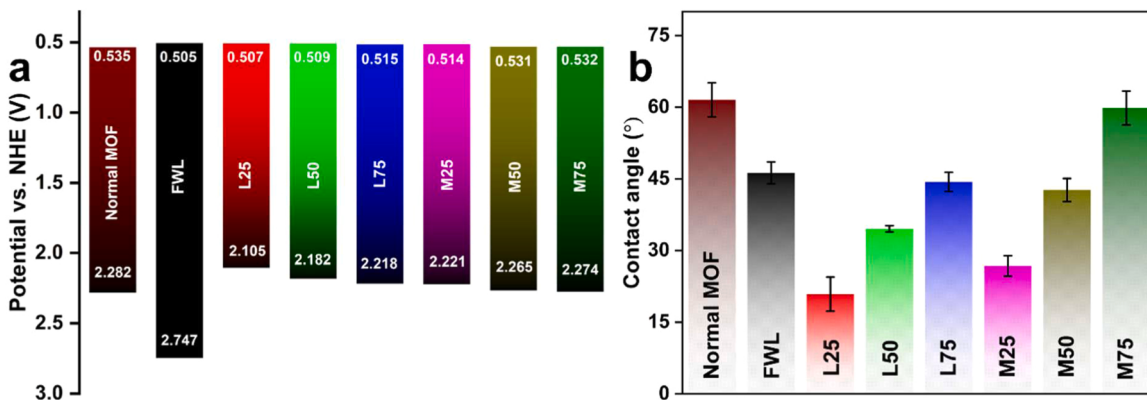


Fig. 8. (a) Schematic illustration of the position of VB-CB for the synthesized materials analysed from Mott Schottky and UV-DRS analysis (b) contact angle of synthesized materials.

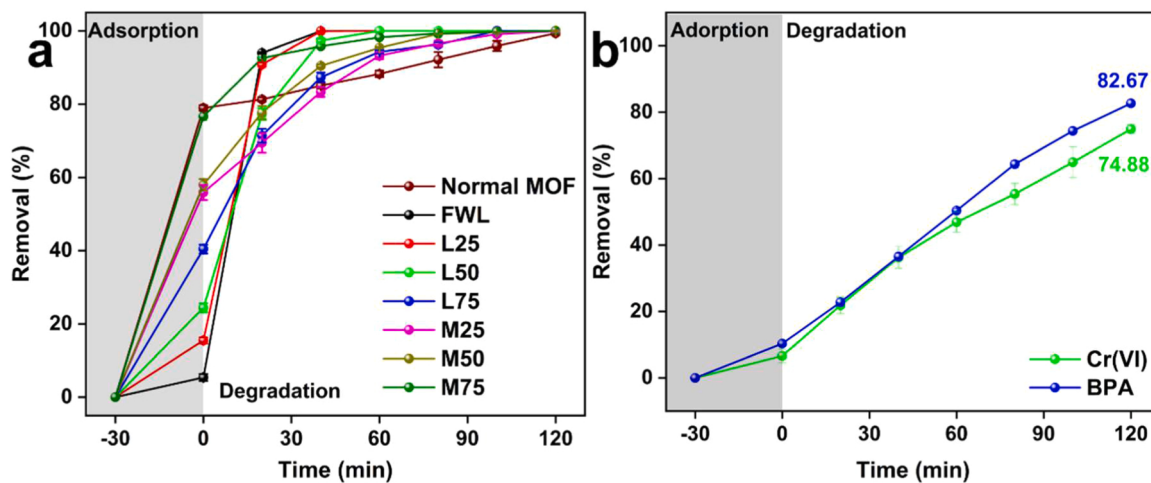


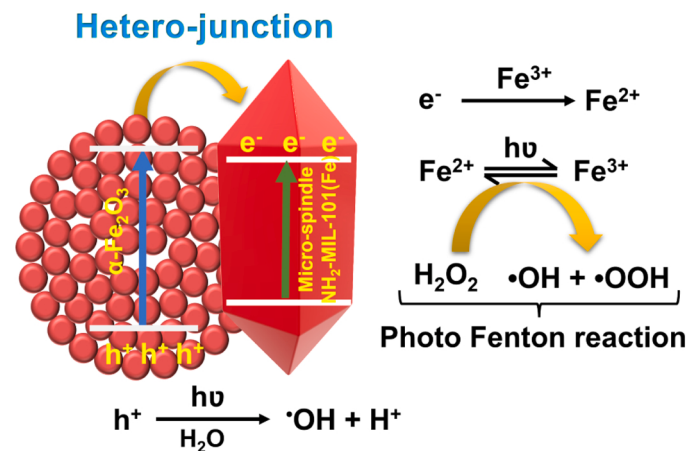
Fig. 9. Photocatalytic (a) degradation of MB dye for synthesized materials (b) Cr(VI) reduction and BPA degradation using L25.

counterpart provides more functional group or metal sites, inducing more hydrophilicity. More hydrophilicity in these deficient materials facilitates better photocatalytic activity as can be seen in ahead sections.

### 3.2. Photocatalytic performance

MB is a popular and model organic dye that can be used to test the photocatalytic performance of materials [43] and hence was used to evaluate the performance of these MOF materials. Photocatalytic capacity of various materials towards degradation of MB dye are shown in Fig. 9 (a). Experiments conducted in dark shows the extent of adsorption and, normal MOF shows highest adsorption of dye molecules, while FWL has least adsorption capacity and this can be related to the surface area and porous nature of materials as discussed in BET section. But when it comes to photocatalytic degradation of the dye, FWL shows the highest activity and this is well established previously [28]. Good light absorbing capacity of  $\alpha$ -Fe<sub>2</sub>O<sub>3</sub> and the variable oxidation states of iron encourages quick redox reactions leading to pollutant degradation [44]. Further the presence of oxygen vacancy as evidenced from O1s spectra can also add to superior photocatalytic performance [45]. However it shows lesser stability (discussed ahead). L25 containing this  $\alpha$ -Fe<sub>2</sub>O<sub>3</sub> too favors the degradation. Metal deficiency shows higher adsorption and can be correlated to higher surface area observed from BET studies; its lower degradation capacity reduces as the deficiency decreases and it gains back its photocatalytic activity. So, it can be generalized that inducing ligand deficiency in MOFs is one of the strategies to form in-situ metal oxides which can enhance electronic transitions between the two entities, reduce charge recombination and enhance photocatalytic degradation.

Further adsorption/degradation kinetics, cyclic stability, catalyst recovery percentage of L25 is compared with control (normal MOF and FWL) and the results are depicted in Fig. S14 (a)-(f). Results show that the catalytic performance of FWL is consistent only upto 4 cycles, indicating its photo instability. The consistency is almost ten cycles in normal MOFs but a decrease in efficiency is observed with every added cycle (Fig. S14(a)). However, ~55–70 % of dye removal is observed in the dark which indicate that the removal is driven by adsorption process in normal MOFs. Pore regeneration capability of material appears to be hampering the performance of normal MOF in successive cycles. In case of L25 adsorption is very less and the catalytic consistency as well as degradation efficiency is retained even after 10 cycles as shown in Fig. S14(f). As we have shown below and in our Section 3.2 represented in Fig. S14(d)-(f), the NH<sub>2</sub>-MIL-101(Fe) is highly photostable and water stable, wherein L25 exhibits 100 % photocatalytic degradation even after 10 cycles without being affected. However, we have now taken the



Scheme 2. Equatorial representation of generation of active species from heterojunction of photocatalyst.

FESEM images (Fig. S15) for L25 material after adsorption- photo-degradation and recovery (washed). No obvious changes could be detected on recovery.

The enhanced photocatalytic activity of L25 is tested for other pollutants like reduction of chromium (Cr (VI)) and degradation of bisphenol-A and the results are shown in Fig. 9 (b). Results indicate L25 shows degradation up to 74.8 % and 82.6 % respectively. Reduction of Cr was comparatively low as the experimental pH used here was 7 and we believe it could be increased on lowering pH values as found in our earlier studies by Nayak et al. and Jyothi et. al. [46,47] as Cr exists as negatively charged dichromate in lower pH that can easily adsorb on positively charged catalyst [48].

#### 3.2.1. Elucidation of degradation mechanism

L25 shows higher degradation, with complete degradation occurring within 40 min unlike normal MOF which takes 120 min (Fig. S14(a)). Under the same conditions, FeCl<sub>3</sub> shows very less degradation and addition of H<sub>2</sub>O<sub>2</sub> shows rapid degradation within 20 min (Fig. S16(a)). However, since it is a homogeneous catalyst, it remains in the solution and becomes a threat, and need secondary process to remove the same.

Amine functional groups attached to aromatic rings facilitate a broader range of absorption in the visible region as shown in Fig. S16(b). In addition, it drives the formation of  $\alpha$ -Fe<sub>2</sub>O<sub>3</sub>, it acts as a nucleophile and attracts excess Fe<sup>3+</sup> to form an aggregated of Fe-O (with oxygen of DMF) cluster giving Fe<sub>2</sub>O<sub>3</sub>. The heterogeneous catalyst L25 is

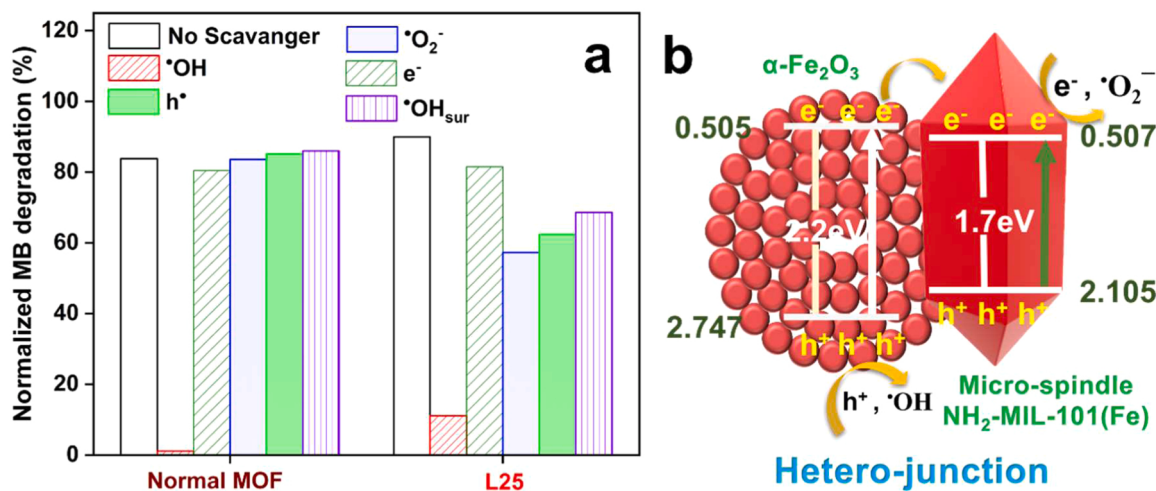


Fig. 10. (a) Scavenger studies on MB degradation using various materials (b) plausible degradation mechanism on L25 (heterojunction).

photoactive, wherein  $\alpha$  -  $\text{Fe}_2\text{O}_3$  in it has an appropriate bandgap of 2.2 eV and responds to illuminated light generating electron hole pair.  $\alpha$  -  $\text{Fe}_2\text{O}_3$  forms a heterojunction with MOF, wherein  $\alpha$  -  $\text{Fe}_2\text{O}_3$  injects its photoexcited electrons into conduction band of MOF as shown in Scheme 2. Thus, a heterojunction is created with  $\text{h}^+$  in VB of  $\alpha$  -  $\text{Fe}_2\text{O}_3$  and  $\text{e}^-$  in CB of MOF allowing good charge separation. This drastically reduces recombination of charge carriers, and subsequently interact with water,  $\text{H}_2\text{O}_2$  and generate reactive species like  $\bullet\text{OH}$ ,  $\bullet\text{O}_2^-$ , thus inducing redox reaction of the pollutant, degrading the pollutant completely. In addition to this, ligand deficiency can lead to extra  $\text{Fe}^{3+}$ , which gets photochemically reduced to  $\text{Fe}^{2+}$  and undergo photo Fenton reaction to generate active species such as  $\bullet\text{OOH}$  and  $\bullet\text{OH}$ . The discussion above is supported with the equations and schematic representation as shown in Scheme 2.

We have also carried out scavenger studies using various scavengers as shown in Fig. S17 and Fig. 10 (a), the figure shows normalized dye degradation after 20 min from the time of addition of specific scavenger. Addition of different reagents like EDTA, *p*-BQ,  $\text{AgNO}_3$ , *tert*-butyl alcohol, and KI are used to scavenge radicals  $\text{h}^+$ ,  $\bullet\text{O}_2$ ,  $\text{e}^-$ ,  $\bullet\text{OH}$ , and  $\bullet\text{OH}_{\text{sur}}$  respectively [42,48]. It can be seen that  $\bullet\text{OH}$  plays a major role in both, normal MOF and L25 and, if scavenged (on addition of *t*-BuOH) will result in almost nil degradation as shown Fig. 10 (a). Fig. S17(b) represents the fall in extent of degradation when various radicals are scavenged. In addition to degradation being affected by  $\bullet\text{OH}$  radicals in L25 we observe the degradation is also affected by  $\bullet\text{O}_2$  and  $\text{h}^+$  radicals indicating the involvement of other radicals generated due to the efficient charge separation achieved in L25. The potential range of energy levels obtained via Mott Schottky analysis for L25 material in Fig. 10 (b) evidently indicates the heterojunction formed in these materials that supports charge separation.

### 3.3. Membrane characterization

Further L25 was experimented for possibility of real time applications, in membrane separation and photodegradation. In this context, electrospun PAN nanofibers were prepared and reduced with hydrazine hydrate [named as rPAN (M1)]. rPAN was further incorporated with L25 (in a stabilized medium of PVA and citric acid) as per the protocol explained in experimental section and it is termed as M2 membrane. It was further characterized to show the presence of L25 in the membranes.

XRD patterns obtained for rPAN (M1) and composite material incorporated PAN (rPAN+L25) (M2) membranes are depicted in Fig. S18. M2 membrane depicts almost all peaks corresponding to L25 (marked in symbols). FESEM images of PAN and reduced PAN

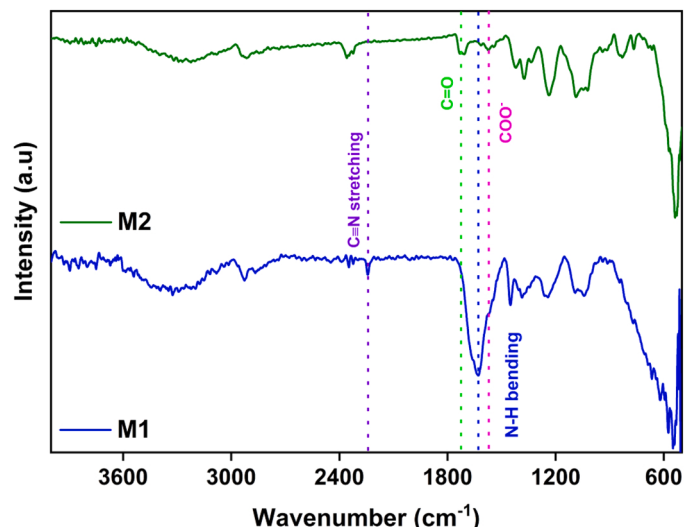


Fig. 11. ATR-IR spectra of membranes, M1 and M2.

nanofibers are given in Fig. S19(a)-(b). rPAN depicts damage free surface and offers higher chemical resistance. Surface and cross-section images of M2 given in Fig. S20(a-f). Fig. S20(a), shows smooth surface without depicting any fibrous nature (even in zoomed inset), indicating a closely packed L25 material (without any surface pores) on the surface. But on intentionally rupturing the surface, nanofibers were spotted along with L25 particles as shown in Fig. S20(b). The cross-section images Fig. S20(c-f) too showed dense packing of fibers emphasizing the role of PVA as binder.

#### 3.3.1. ATR-IR functional group analysis

ATR IR spectra obtained for M1 and M2 membranes are depicted in Fig. 11. M1 membrane shows peak of primary amine (C-N) at 1250 cm<sup>-1</sup> and its N-H bend and stretch vibration at 1630 cm<sup>-1</sup> and at around 3400 cm<sup>-1</sup> respectively for reduced acrylonitrile group. However, all of these peaks disappear in M2 as the surface is completely covered by L25, except for a small peak at 2241 cm<sup>-1</sup> attributed to reduced nitrile group. Peaks corresponding to L25, mainly vibrations of carboxylate (COO<sup>-</sup>), C=O and NH at 1571 cm<sup>-1</sup>, 1710 cm<sup>-1</sup> and 1625 cm<sup>-1</sup> could be clearly identified in M2.

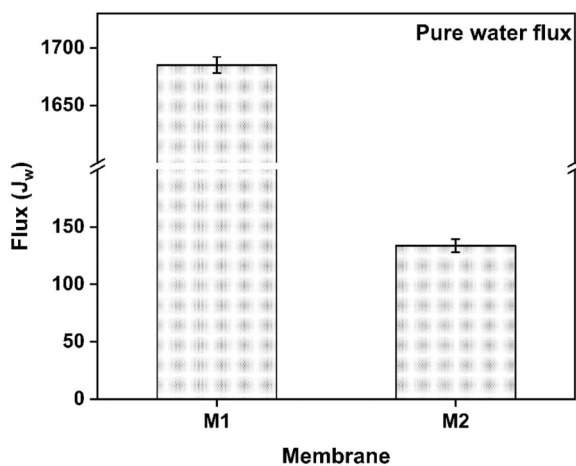


Fig. 12. Pure water flux of membranes.

#### 3.4. Membrane performance studies

The pure water flux study conducted for M1 and M2 is illustrated in Fig. 12. M1 shows higher flux (pressure of  $\sim 0.2$  bar) due to high porosity in randomly aligned nanofibers [42]. The coating of photocatalytic material (L25) on the surface via vacuum filtration significantly reduces the flux due to compact packing of L25 as can be seen in FESEM images.

In order to evaluate the simultaneous membrane rejection and degradation performance, MB dye (10 ppm) is used as a model pollutant and the results observed are depicted in Fig. 13(a-b). Fig. 14(a) shows

results of filtration study without light, and M1 membrane shows poor rejection efficiency of 8.5 % with a huge permeate flux of  $1632 \text{ L/m}^2/\text{h}$  while M2, shows high rejection efficiency of 73.5 % and this massive increase is due to L25 which act as nano filters for MB dye molecules and allows mostly water molecules to permeate [49]. Further a tremendous increase in rejection to 93.6 % can be achieved on exposing the membrane to light and Fig. 13(b) shows this coupled process of simultaneous separation and photo-catalytic degradation of dye which enhances the rejection efficiency by 20 % and this is attributed to photocatalytic degradation. The flux also increased considerably from 118.5 to  $125.6 \text{ L/m}^2/\text{h}$  for photocatalytic separation process. This suggests that the absorbed dye molecules on L25 material gets degraded thus allowing the membrane to undergo self-cleaning process, thus contributing to higher flux and rejection.

From the literature it is found that Lu et al. fabricated Ag@AgCl@MIL-100(Fe) MOF on photocatalytic cellulose nanofibers via in-situ synthesis and achieved huge flux of  $4927 \text{ L/m}^2/\text{h}$ . The fabricated membrane also provides high removal efficiency of  $\approx 99\%$  via adsorption. However post-treatment was necessary to desorb and degrade the pollutants under light sources. Most of the filtration studies using nanofiber membrane is based on adsorption separation and post-photodegradation process as summarized in Table 1. However, in our study we couple both separation and degradation together for enhanced separation, degradation and mitigation of fouling in membranes and it was difficult to find any earlier reports which had such coupled, simultaneous processes for comparison.

Leaching of particles could not be detected due to the tightly packed water stabilized PVA-citric acid polymer chains that allows the L25 material to strongly bind to nanofibers and this study was previously conducted elaborately by us, because of which we have used PVA and citric acid here in this study [50].

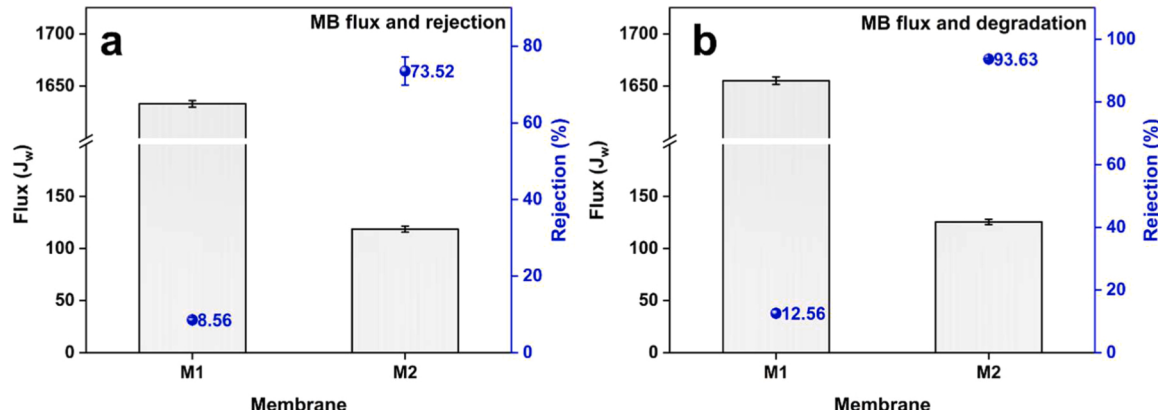


Fig. 13. (a) MB flux and rejection (b) MB flux and rejection-photo degradation using membranes.

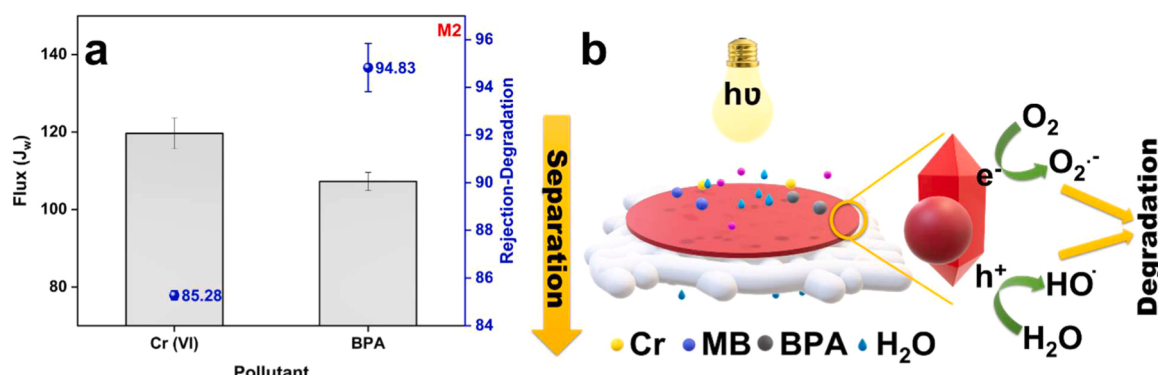
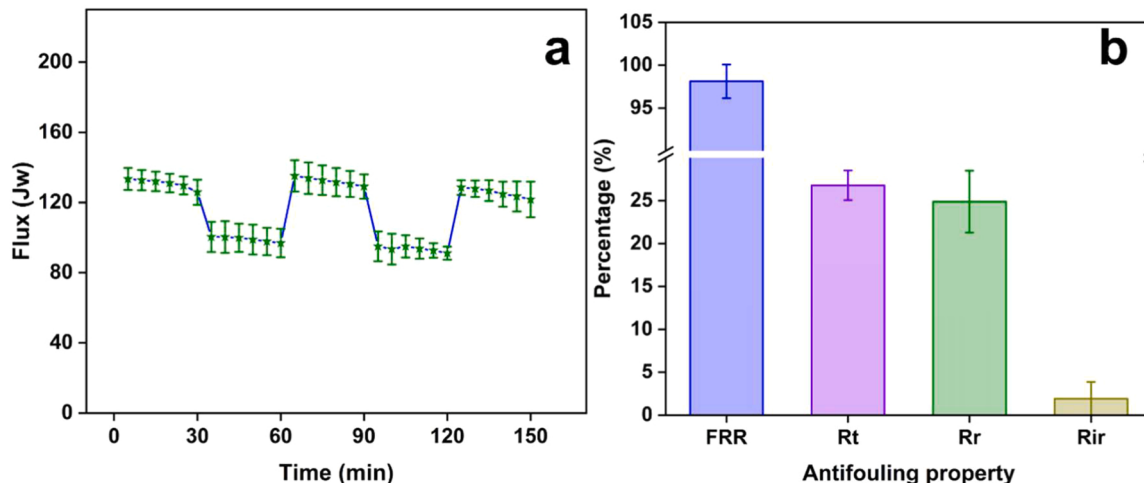


Fig. 14. (a) Cr(VI) and BPA rejection and photodegradation using M2 membrane (b) schematic of photocatalytic separation principle in the fabricated membranes.

**Table 1**

Photocatalytic nanofiber membrane fabrication and its removal efficiency.

Nanofiber membrane	Fabrication route	Pollutant and removal route	Degradation	Removal efficiency with flux	Antifouling capability (Irreversible fouling)	Ref. No.
Hydrolyzed PAN with MIL-88B(Fe)	Self-assembly	Oil-water separation Rhodamine B adsorption	Post-degradation under 300 W Xe lamp	<99 % (946 L/m <sup>2</sup> /h)	12.4 %	[51]
ZnO/Ag/β-CD/PAN	in-situ hydrothermal synthesis method.	Mixture of Oil-water methylene blue (MB) and congo red (CR) separation. MB & CR adsorption degradation	Post-degradation under sunlight	<99 % (>1100 L/m <sup>2</sup> /h)	-	[52]
CS/PAN@FeOOH/g-C <sub>3</sub> N <sub>4</sub>	Blending and spinning	MB and Erythromycin (ERY) adsorption and Fenton degradation	Post-degradation under 300 W Xe lamp	68.7 % (35.6 LMH•psi)	13.8 %	[53]
rPAN@L25	Vacuum fabrication	MB rejection and degradation. (One of the pollutant result is depicted)	Simultaneous separation and degradation under 125 W mercury vapor lamp	MB – 93.63 % (125.6 L/m <sup>2</sup> /h)	<2 %	This work

**Fig. 15.** Anti-fouling study (a) Water and BSA flux (b) calculated fouling parameters.

The same trend can be observed in separation of Cr (VI) and BPA and the results are given in Fig. 14 (a). Surprisingly the enhancement in extent of degradation is higher in this coupled process by almost 10 % over the photocatalytic process carried out with free standing particles and we predict the bigger size of BPA and Cr complex (formed in-situ) to be the reason behind this and a more in-depth study needs to be done to provide better insights into this. Fig. 15 (b) illustrates the schematic of simultaneous separation and degradation performed using the fabricated membrane.

#### 3.4.1. Antifouling studies

Antifouling study was conducted for M2 membrane to understand the interaction of membrane with pollutants. Accordingly, the anti-fouling characteristics of the fabricated membrane was investigated using alternative cycles of water and BSA rejection, continuously for 2.5 h and the obtained result is depicted in Fig. 15 (a-b). The BSA rejection conducted for two cycles is illustrated in Fig. S21. Results emphasize very minimal fouling and flux recovery ratio is high (>95 %), with irreversible fouling being less than 2 %, and this indicates that these membranes are highly resistant to foulants and are capable of being regenerated almost completely. Table 1 depicts the comparison of irreversible fouling exhibited by various membranes, applied to such separation and degradation, reported previously in a review [54] and the present work shows a very low value. Thus, these membranes can repeatedly be used and they also have the potential to undergo self-cleaning. This could be because of the enormous functional groups like NH<sub>2</sub> and ester linkages of L25 present on membrane surface, that prevent foulant deposition [54].

#### 4. Conclusion

In summary, a combination of NH<sub>2</sub>-MIL-101(Fe) MOF and α-Fe<sub>2</sub>O<sub>3</sub> is synthesized via one-pot solvothermal method by applying the stoichiometric deficiency strategy of reticular chemistry. Freely accessible amine groups of deficient MOFs drive the formation of α-Fe<sub>2</sub>O<sub>3</sub> via the excess metal precursor. Different sizes and morphology of NH<sub>2</sub>-MIL-101 (Fe) observed during such stoichiometric variation in precursors, emphasizes the necessity of optimization for any MOF synthesis. It is believed that this strategy can be extended to synthesize various metal oxides along with MOFs by tuning the precursor concentration and choosing appropriate solvent medium for a wide range of applications and not limited to hydrogen evolution reaction, photovoltaics and sensors. Photocatalytic studies suggest that the ligand based stoichiometric deficiency which facilitates a composite of MO-MOF with a heterojunction facilitates good charge separation for pollutant degradation. In addition, the easy route of fabricating L25 incorporated or surface functionalized nanofibers yielded a simultaneous membrane-based separation and photodegradation successfully.

#### CRediT authorship contribution statement

**Karthikeyarajan Vinothkumar:** Conceptualization, Methodology, Software, Validation, Formal analysis, Data curation, Writing – original draft, Visualization, Project administration. **R Geetha Balakrishna:** Validation, Investigation, Resources, Writing – review & editing, Visualization, Supervision, Funding acquisition.

## Declaration of Competing Interest

The authors state that they have no conflicting financial interests or personal ties that has influenced the work reported in this research.

## Data availability

Data will be made available on request.

## Acknowledgement

Authors would like to acknowledge Department of Science and Technology, Government of India for the financial support DST/TMD/(EWO)/OWUIS-2018/RS-14 (G).

## Appendix A. Supporting information

Supplementary data associated with this article can be found in the online version at [doi:10.1016/j.apcatb.2023.123199](https://doi.org/10.1016/j.apcatb.2023.123199).

## References

- H. Li, M. Eddaoudi, M. O'Keeffe, O.M. Yaghi, Design and synthesis of an exceptionally stable and highly porous metal-organic framework, *Nature* 402 (1999) 276–279, <https://doi.org/10.1038/46248>.
- H. Furukawa, K.E. Cordova, M. O'Keeffe, O.M. Yaghi, The chemistry and applications of metal-organic frameworks, *Science* 341 (2013) 1230444, <https://doi.org/10.1126/science.1230444>.
- H.-C. Zhou, J.R. Long, O.M. Yaghi, Introduction to metal-organic frameworks, *Chem. Rev.* 112 (2012) 673–674, <https://doi.org/10.1021/cr300014x>.
- Q. Wang, D. Astruc, State of the art and prospects in metal-organic framework (MOF)-based and MOF-derived nanocatalysis, *Chem. Rev.* 120 (2020) 1438–1511, <https://doi.org/10.1021/acs.chemrev.9b00223>.
- Z. Zhang, M.J. Zaworotko, Template-directed synthesis of metal-organic materials, *Chem. Soc. Rev.* 43 (2014) 5444–5455, <https://doi.org/10.1039/C4CS00075G>.
- J. Hwang, R. Yan, M. Oschatz, B.V.K.J. Schmidt, Solvent mediated morphology control of zinc MOFs as carbon templates for application in supercapacitors, *J. Mater. Chem. A* 6 (2018) 23521–23530, <https://doi.org/10.1039/C8TA07700B>.
- G. Majano, O. Martin, M. Hammes, S. Smeets, C. Baerlocher, J. Pérez-Ramírez, Solvent-mediated reconstruction of the metal-organic framework HKUST-1 ( $\text{Cu}_3(\text{BTC})_2$ ), *Adv. Funct. Mater.* 24 (2014) 3855–3865, <https://doi.org/10.1002/adfm.201303678>.
- Y. Niu, Y. Yuan, Q. Zhang, F. Chang, L. Yang, Z. Chen, Z. Bai, Morphology-controlled synthesis of metal-organic frameworks derived lattice plane-altered iron oxide for efficient trifunctional electrocatalysts, *Nano Energy* 82 (2021), 105699, <https://doi.org/10.1016/j.nanoen.2020.105699>.
- M.J. Kalmutzki, N. Hanikel, O.M. Yaghi, Secondary building units as the turning point in the development of the reticular chemistry of MOFs, *Sci. Adv.* 4 (2018), eaat9180, <https://doi.org/10.1126/sciadv.aat9180>.
- S.S. Park, C.H. Hendon, A.J. Fielding, A. Walsh, M. O'Keeffe, M. Dincă, The organic secondary building unit: strong intermolecular  $\pi$  interactions define topology in MIT-25, a mesoporous MOF with proton-replete channels, *J. Am. Chem. Soc.* 139 (2017) 3619–3622, <https://doi.org/10.1021/jacs.6b13176>.
- L. Yu, S. Ullah, K. Zhou, Q. Xia, H. Wang, S. Tu, J. Huang, H.-L. Xia, X.-Y. Liu, T. Thonhauser, J. Li, A microporous metal-organic framework incorporating both primary and secondary building units for splitting alkane isomers, *J. Am. Chem. Soc.* 144 (2022) 3766–3770, <https://doi.org/10.1021/jacs.1c12068>.
- Z. Ji, T. Li, O.M. Yaghi, Sequencing of metals in multivariate metal-organic frameworks, *Science* 369 (2020) 674–680, <https://doi.org/10.1126/science.aae4304>.
- S. Pullen, G.H. Clever, Mixed-ligand metal-organic frameworks and heteroleptic coordination cages as multifunctional scaffolds—a comparison, *Acc. Chem. Res.* 51 (2018) 3052–3064, <https://doi.org/10.1021/acs.accounts.8b00415>.
- T. Xue, T. He, L. Peng, O.A. Syzgantseva, R. Li, C. Liu, D.T. Sun, G. Xu, R. Qiu, Y. Wang, S. Yang, J. Li, J.-R. Li, W.L. Queen, A customized MOF-polymer composite for rapid gold extraction from water matrices, *Sci. Adv.*, 9, eadg4923, <https://doi.org/10.1126/sciadv.adg4923>.
- S. Naghdi, A. Cherevan, A. Giesriegl, R. Guillet-Nicolas, S. Biswas, T. Gupta, J. Wang, T. Haunold, B.C. Bayer, G. Rupprechter, M.C. Toroker, F. Kleitz, D. Eder, Selective ligand removal to improve accessibility of active sites in hierarchical MOFs for heterogeneous photocatalysis, *Nat. Commun.* 13 (2022) 282, <https://doi.org/10.1038/s41467-021-27775-7>.
- S.J. Datta, A. Mayoral, N. Murthy Srivatsa Bettahalli, P.M. Bhatt, M. Karunakaran, I.D. Carja, D. Fan, P. Graziante, M. Mileo, R. Semino, G. Maurin, O. Terasaki, M. Eddaoudi, Rational design of mixed-matrix metal-organic framework membranes for molecular separations, *Science* 376 (2022) 1080–1087, <https://doi.org/10.1126/science.abe0192>.
- M. Viciano-Chumillas, X. Liu, A. Leyva-Pérez, D. Armentano, J. Ferrando-Soria, E. Pardo, Mixed component metal-organic frameworks: Heterogeneity and complexity at the service of application performances, *Coord. Chem. Rev.* 451 (2022), 214273, <https://doi.org/10.1016/j.ccr.2021.214273>.
- Y. Yang, Z. Zheng, W. Ji, J. Xu, X. Zhang, Insights to perfluoroctanoic acid adsorption micro-mechanism over Fe-based metal organic frameworks: Combining computational calculation with response surface methodology, *J. Hazard. Mater.* 395 (2020), 122686, <https://doi.org/10.1016/j.jhazmat.2020.122686>.
- K. Vinothkumar, M. Shivantha Jyothi, C. Lavanya, M. Sakar, S. Valiyaveettil, R. G. Balakrishna, Strongly co-ordinated MOF-PSF matrix for selective adsorption, separation and photodegradation of dyes, *J. Chem. Eng.* 428 (2022), 132561, <https://doi.org/10.1016/j.cej.2021.132561>.
- K.G.M. Laurier, F. Vermoortele, R. Ameloot, D.E. De Vos, J. Hofkens, M.B. J. Roefaaers, Iron(III)-based metal-organic frameworks as visible light photocatalysts, *J. Am. Chem. Soc.* 135 (2013) 14488–14491, <https://doi.org/10.1021/ja405086e>.
- C. Du, Y. Zhang, Z. Zhang, L. Zhou, G. Yu, X. Wen, T. Chi, G. Wang, Y. Su, F. Deng, Y. Lv, H. Zhu, Fe-based metal organic frameworks (Fe-MOFs) for organic pollutants removal via photo-Fenton: a review, *J. Chem. Eng.* 431 (2022), 133932, <https://doi.org/10.1016/j.cej.2021.133932>.
- K. Li, Y. de Rancourt de Mimérand, X. Jin, J. Yi, J. Guo, Metal oxide ( $\text{ZnO}$  and  $\text{TiO}_2$ ) and Fe-based metal-organic-framework nanoparticles on 3D-printed fractal polymer surfaces for photocatalytic degradation of organic pollutants, *ACS Appl. Nano Mater.* 3 (2020) 2830–2845, <https://doi.org/10.1021/acsnano.0c00096>.
- C. Yang, Y. Zhu, J. Wang, W. Sun, L. Yang, H. Lin, S. Lv, A novel granular MOF composite with dense and ordered MIL-100(Fe) nanoparticles grown on porous alumina: green synthesis and enhanced adsorption of tetracycline hydrochloride, *J. Chem. Eng.* 426 (2021), 131724, <https://doi.org/10.1016/j.cej.2021.131724>.
- M. Huang, L. Wang, K. Pei, W. You, X. Yu, Z. Wu, R. Che, Multidimension-controllable synthesis of MOF-derived Co@N-doped carbon composite with magnetic-dielectric synergy toward strong microwave absorption, *Small* 16 (2020), 2000158, <https://doi.org/10.1002/smll.202000158>.
- L. Shi, T. Wang, H. Zhang, K. Chang, X. Meng, H. Liu, J. Ye, An amine-functionalized iron(III) metal-organic framework as efficient visible-light photocatalyst for Cr(VI) reduction, *Adv. Sci.* 2 (2015), 1500006, <https://doi.org/10.1002/advs.201500006>.
- D. Wang, R. Huang, W. Liu, D. Sun, Z. Li, Fe-based MOFs for photocatalytic  $\text{CO}_2$  reduction: role of coordination unsaturated sites and dual excitation pathways, *ACS Catal.* 4 (2014) 4254–4260, <https://doi.org/10.1021/cs501169t>.
- M. Rioult, D. Stancescu, E. Fonda, A. Barbier, H. Magnan, Oxygen vacancies engineering of iron oxides films for solar water splitting, *J. Phys. Chem. C* 120 (2016) 7482–7490, <https://doi.org/10.1021/acs.jpcc.6b00552>.
- J. Lian, X. Duan, J. Ma, P. Peng, T. Kim, W. Zheng, Hematite ( $\alpha\text{-Fe}_2\text{O}_3$ ) with various morphologies: ionic liquid-assisted synthesis, formation mechanism, and properties, *ACS Nano* 3 (2009) 3749–3761, <https://doi.org/10.1021/nn090041e>.
- X. Zhang, C. Sui, J. Gong, Z. Su, L. Qu, Preparation and formation mechanism of different  $\alpha\text{-Fe}_2\text{O}_3$  morphologies from snowflake to paired microplates, dumbbell, and spindle microstructures, *J. Phys. Chem. C* 111 (2007) 9049–9054, <https://doi.org/10.1021/jp0688310>.
- S.-W. Lv, J.-M. Liu, C.-Y. Li, N. Zhao, Z.-H. Wang, S. Wang, A novel and universal metal-organic frameworks sensing platform for selective detection and efficient removal of heavy metal ions, *J. Chem. Eng.* 375 (2019), 122111, <https://doi.org/10.1016/j.cej.2019.122111>.
- L. Chandra, K. Vinothkumar, R.G. Balakrishna, MIL-100 (Fe) integrated fibrous polyvinyl alcohol graft on cellulose acetate towards the development of green membranes: application in multi solute rejection, *J. Environ. Chem. Eng.* 11 (2023), 109851, <https://doi.org/10.1016/j.jece.2023.109851>.
- M.A. Siregar, J.A. Santri, D. Aksani, A. Maas, M. Nurudin, Analysis of FTIR spectroscopic data to observe hydrophilic and hydrophobic levels of peat in hemic and sapric maturity, *IOP Conf. Ser. Earth Environ. Sci.* 1025 (2022), 012026, <https://doi.org/10.1088/1755-1315/1025/1/012026>.
- K.I. Hadjiivanov, D.A. Panayotov, M.Y. Miyaylov, E.Z. Ivanova, K.K. Chakarova, S. M. Andonova, N.L. Drenchev, Power of infrared and Raman spectroscopies to characterize metal-organic frameworks and investigate their interaction with guest molecules, *Chem. Rev.* 121 (2021) 1286–1424, <https://doi.org/10.1021/acs.chemrev.0c00487>.
- Q. Xie, Y. Li, Z. Lv, H. Zhou, X. Yang, J. Chen, H. Guo, Effective adsorption and removal of phosphate from aqueous solutions and eutrophic water by Fe-based MOFs of MIL-101, *Sci. Rep.* 7 (2017) 3316, <https://doi.org/10.1038/s41598-017-03526-x>.
- F. Ambroz, T.J. Macdonald, V. Martis, I.P. Parkin, Evaluation of the BET theory for the characterization of meso and microporous MOFs, *Small Methods* 2 (2018) 1800173, <https://doi.org/10.1002/smtd.201800173>.
- C. Wang, T. Wang, B. Wang, X. Zhou, X. Cheng, P. Sun, J. Zheng, G. Lu, Design of  $\alpha\text{-Fe}_2\text{O}_3$  nanorods functionalized tubular  $\text{NiO}$  nanostructure for discriminating toluene molecules, *Sci. Rep.* 6 (2016) 26432, <https://doi.org/10.1038/srep26432>.
- R. Azuma, S. Nakamichi, J. Kimura, H. Yano, H. Kawasaki, T. Suzuki, R. Kondo, Y. Kanda, K.-i. Shimizu, K. Kato, Y. Obora, Solution synthesis of N,N-dimethylformamide-stabilized iron-oxide nanoparticles as an efficient and recyclable catalyst for alkene hydroxylation, *ChemCatChem* 10 (2018) 2378–2382, <https://doi.org/10.1002/cctc.201800161>.
- Y. Ma, Y. Lu, G. Hai, W. Dong, R. Li, J. Liu, G. Wang, Bidentate carboxylate linked  $\text{TiO}_2$  with NH2-MIL-101(Fe) photocatalyst: a conjugation effect platform for high photocatalytic activity under visible light irradiation, *Sci. Bull.* 65 (2020) 658–669, <https://doi.org/10.1016/j.scib.2020.02.001>.
- M.C. Biesinger, B.P. Payne, A.P. Grosvenor, L.W.M. Lau, A.R. Gerson, R.S.C. Smart, Resolving surface chemical states in XPS analysis of first row transition metals,

oxides and hydroxides: Cr, Mn, Fe, Co and Ni, *Appl. Surf. Sci.* 257 (2011) 2717–2730, <https://doi.org/10.1016/j.apsusc.2010.10.051>.

[40] Q. Qin, T. Liu, J. Zhang, R. Wei, S. You, Y. Xu, Facile synthesis of oxygen vacancies enriched  $\alpha$ -Fe2O3 for peroxymonosulfate activation: a non-radical process for sulfamethoxazole degradation, *J. Hazard. Mater.* 419 (2021), 126447, <https://doi.org/10.1016/j.jhazmat.2021.126447>.

[41] A. Hankin, F.E. Bedoya-Lora, J.C. Alexander, A. Regoutz, G.H. Kelsall, Flat band potential determination: avoiding the pitfalls, *J. Mater. Chem. A* 7 (2019) 26162–26176, <https://doi.org/10.1039/C9TA09569A>.

[42] Y. Nosaka, A.Y. Nosaka, Generation and detection of reactive oxygen species in photocatalysis, *Chem. Rev.* 117 (2017) 11302–11336, <https://doi.org/10.1021/acs.chemrev.7b00161>.

[43] M. Rashad, N.M. Shaalan, A.M. Abd-Elnaiem, Degradation enhancement of methylene blue on ZnO nanocombs synthesized by thermal evaporation technique, *Desalin. Water Treat.* 57 (2016) 26267–26273, <https://doi.org/10.1080/19443994.2016.1163511>.

[44] M. Mishra, D.-M. Chun,  $\alpha$ -Fe2O3 as a photocatalytic material: a review, *Appl. Catal. A Gen.* 498 (2015) 126–141, <https://doi.org/10.1016/j.apcata.2015.03.023>.

[45] N. Zhang, Q. Zhang, L.-Y. Zhang, J.-Y. Zhang, Y.-Z. Fang, Z. Liu, M. Zhou, Oxygen vacancy induced boosted visible-light driven photocatalytic CO<sub>2</sub> reduction and electrochemical water oxidation over CuCo-ZIF@Fe2O3@CC Architecture, *Small Methods* 6 (2022), 2200308, <https://doi.org/10.1002/smtd.202200308>.

[46] J.M.S., V. Nayak, M. Padaki, R.G. Balakrishna, K. Soontarapa, Eco-friendly membrane process and product development for complete elimination of chromium toxicity in wastewater, *J. Hazard. Mater.* 332 (2017) 112–123, <https://doi.org/10.1016/j.jhazmat.2017.03.009>.

[47] V. Nayak, M.S. Jyothi, R.G. Balakrishna, M. Padaki, A.F. Ismail, Preparation and characterization of chitosan thin films on mixed-matrix membranes for complete removal of chromium, *ChemistryOpen* 4 (2015) 278–287, <https://doi.org/10.1002/open.201402133>.

[48] J.T. Schneider, D.S. Firak, R.R. Ribeiro, P. Peralta-Zamora, Use of scavenger agents in heterogeneous photocatalysis: truths, half-truths, and misinterpretations, *Phys. Chem. Chem. Phys.* 22 (2020) 15723–15733, <https://doi.org/10.1039/DQCP02411B>.

[49] J. Xue, T. Wu, Y. Dai, Y. Xia, Electrospinning and electrospun nanofibers: methods, materials, and applications, *Chem. Rev.* 119 (2019) 5298–5415, <https://doi.org/10.1021/acs.chemrev.8b00593>.

[50] D. Wood, S. Shaw, T. Cawte, E. Shanen, B. Van Heyst, An overview of photocatalyst immobilization methods for air pollution remediation, *J. Chem. Eng.* 391 (2020), 123490, <https://doi.org/10.1016/j.cej.2019.123490>.

[51] B. Li, J. Zhao, X. Lin, D. Tu, Y. Meng, Y. Li, P. Huang, H. Zhang, Highly efficient sunlight-driven self-cleaning electrospun nanofiber membrane NM88B@HPAN for water treatment, *J. Clean. Prod.* 355 (2022), 131812, <https://doi.org/10.1016/j.jclepro.2022.131812>.

[52] W. Cao, W. Ma, T. Lu, Z. Jiang, R. Xiong, C. Huang, Multifunctional nanofibrous membranes with sunlight-driven self-cleaning performance for complex oily wastewater remediation, *J. Colloid Interface Sci.* 608 (2022) 164–174, <https://doi.org/10.1016/j.jcis.2021.09.194>.

[53] S. Zheng, H. Chen, X. Tong, Z. Wang, J.C. Crittenden, M. Huang, Integration of a photo-Fenton reaction and a membrane filtration using CS/PAN@FeOOH/g-C3N4 electrospun nanofibers: synthesis, characterization, self-cleaning performance and mechanism, *Appl. Catal. B Environ.* 281 (2021), 119519, <https://doi.org/10.1016/j.apcatb.2020.119519>.

[54] V. Nayak, J. Mannekote Shivanna, S. Ramu, S. Radoor, R.G. Balakrishna, Efficacy of electrospun nanofiber membranes on fouling mitigation: a review, *ACS Omega* 7 (2022) 43346–43363, <https://doi.org/10.1021/acsomega.2c02081>.